

Supplementary Materials for  
Photoluminescence Lifetimes Exceeding 8  $\mu$ s  
and Quantum Yields Exceeding 30% in Hybrid  
Perovskite Thin Films by Ligand Passivation

*Dane W. deQuilettes<sup>1</sup>, Susanne Koch<sup>1,2</sup>, Sven Burke<sup>1</sup>, Rajan K. Paranjji<sup>1</sup>, Alfred J. Shropshire<sup>1</sup>, Mark E. Ziffer<sup>1</sup>, David S. Ginger<sup>1\*</sup>*

<sup>1</sup>Department of Chemistry, University of Washington, Box 351700, Seattle, Washington 98195-1700, United States

<sup>2</sup>Present Address: Department of Physics, University of Konstanz, P.O. Box 680, 78457 Konstanz, Germany

**\*Corresponding Author:** ginger@chem.washington.edu

## Materials and Methods

### Perovskite Precursor Preparation

#### *PbOAc<sub>2</sub> as a Pb Source*

A methylammonium iodide (MAI) stock solution was made by dissolving MAI (Dyesol, CAS:14965-49-2) in anhydrous *N,N*-dimethylformamide (DMF) at a concentration of 1.78 M. Then lead acetate trihydrate (99.999%, Sigma-Aldrich, CAS:6080-56-4) was added at a 3:1 molar ratio of MAI to PbOAc<sub>2</sub>·3 H<sub>2</sub>O (0.59 M).<sup>1</sup> All solutions were made in a nitrogen filled glovebox.

#### *PbCl<sub>2</sub> and PbI<sub>2</sub> as Pb Sources*

Methylammonium iodide (MAI) was prepared by reacting methylamine, 33 wt% in ethanol (Sigma-Aldrich), with hydroiodic acid (HI) 57 wt% in water (Sigma-Aldrich), at room temperature. HI was added dropwise while stirring. MAI was precipitated out of solution by heating the solution at 100 °C overnight to drive off the solvent. The crude MAI was either used without further purification or recrystallized in a mixed solvent of ethanol and ether.

To form the non-stoichiometric CH<sub>3</sub>NH<sub>3</sub>PbI<sub>3</sub>(Cl) precursor solution, MAI and lead (II) chloride (99.999%, Sigma-Aldrich) were dissolved in DMF at a 3:1 molar ratio of MAI to PbCl<sub>2</sub>, with final concentrations 0.88 M lead chloride and 2.64 M methylammonium iodide.<sup>2</sup> This solution was stored under a dry nitrogen atmosphere.

To form the CH<sub>3</sub>NH<sub>3</sub>PbI<sub>3</sub> precursor solution, MAI and PbI<sub>2</sub> (Sigma) were dissolved in a mixed solvent of dimethylsulfoxide and  $\gamma$ -butyrolactone (volume ratio of 3:7) at a 1:1 molar ratio of MAI to PbI<sub>2</sub>, with final concentrations of 1 M and stirred at 60 °C for 12 h.<sup>3</sup>

### Perovskite Deposition

First, glass substrates were cleaned sequentially in 2% Micro-90 detergent, acetone, then propan-2-ol. To form the perovskite layer for spectroscopy measurements, the precursor solutions were spin-coated on plasma-cleaned substrates in a nitrogen-filled glovebox, at 2000 rpm for 60 s.

Films prepared from the PbOAc<sub>2</sub> precursor were left to dry at room temperature in the glovebox for 10 minutes and then annealed on a hotplate at 100 °C for 5 minutes.

Films prepared from the PbCl<sub>2</sub> precursor were left at room temperature in the glovebox for 30 minutes and then annealed on a hotplate in the glovebox at 90 °C for 150 minutes.

Films prepared from the PbI<sub>2</sub> precursor were prepared using the “dripping” method, where the perovskite precursor was filtered through a 0.22  $\mu$ m PTFE filter onto the glass substrate and spin coated at 1000 rpm for 15 s and then 4000 rpm for 45 s. During the last

15 s of the second spin-coating step, the substrate was treated with toluene drop-casting (0.7 mL). The resulting thin films were annealed at 100 °C for 10 min.<sup>3</sup> All films were then encapsulated in a nitrogen atmosphere with vacuum grease and clean microscope coverslips.

### Surface Treatment Deposition and Wash

All treatment solutions reported in the main article were prepared in anhydrous chlorobenzene (Sigma-Aldrich, CAS: 108-90-7) with concentration ranges from 0.005 M to 0.087 M. Other treatments not reported in the main article (Figure S1 and Table S1) were also prepared in anhydrous chlorobenzene with concentration ranges from 0.002 M to 1 M. Nearly all chemical treatments were readily solvated in CB, but a few treatments required further agitation via vortexing or sonication for ~ 10 min. Treatments were carried out by depositing ~70  $\mu$ L of the treatment solution on the film then immediately spincoating at 2000 rpm for 60 s. Higher concentration treatments (> 0.025 M) can often leave a filmy residue on the surface, which can be removed with a dynamic solvent wash while still maintaining PL improvements (Figure S4) and film morphology (Figure S6). A “dynamic” wash involves depositing 40  $\mu$ L of anhydrous CB or 2-propanol (IPA) onto the perovskite film while it is already rotating at 6000 rpm for 45 s, while in a “regular” wash, CB or IPA is deposited before starting the spincoating procedure at 2000 rpm for 30 s.

## **Characterization**

### Scanning Electron Microscopy (SEM)

SEM images were taken using a FEI Sirion SEM at 5 kV accelerating voltage. To prevent charging effects, samples for SEM were imaged after sputtering approximately 7 nm of Au/Pd using a SPI-Module Sputter Coater with argon flow.

### X-ray Diffraction Spectroscopy

Diffractograms were collected on a Bruker D8 Discover with GADDS XRD system. The X-ray source was a Cu rotating anode operating at 5.4 kW in collimated beam geometry ( $K\alpha$  only) with an 800  $\mu$ m beam diameter. Diffracted X-rays were collected using a Bruker Hi-Star 2D area detector, at distance of 20 cm from the sample.

### Glow Discharge Optical Emission Spectroscopy (GDOES)

Depth-dependent compositional profiles were collected with a Horiba GD-Profiler-2 using a high-power radio frequency (RF) argon plasma in a 4 mm diameter anode. The plasma was operated at 30 W and a pressure of 600 Pa. Sulfur (S) and lead (Pb) were detected using the 181 nm and 406 nm atomic emission lines, respectively. Time zero was defined as the time at which the reflected plasma power stabilized. Samples were first treated with 0.087 M ODT in anhydrous CB, then dynamically washed with CB or IPA at 6000 rpm for 45 s to remove excess unreacted ligand. After the washing step,

there appeared to be no residual unreacted ODT on the surface via SEM (Figure S6), and the sample maintained a PL improvement relative to the control film (Figure S4), which showed no significant sulfur (S) content as observed via GDOES (Figure S5).

### Nuclear Magnetic Resonance (NMR) Spectroscopy

1D  $^{31}\text{P}$  solid state NMR spectra were recorded on a Bruker AV-III spectrometer at a Larmor frequency of 283.394 MHz, using a standard cross-polarization (CP) pulse sequence with  $^1\text{H}$  decoupling. Both the  $\text{PPh}_3$  control as well as perovskite samples were prepared by making fine powders that were packed densely into 3.2 mm magic angle spinning (MAS) rotors. Data were obtained using a Bruker  $^1\text{H}\{^{13}\text{C}, ^{31}\text{P}\}$  triple resonance MAS probehead with a rotor spinning rate of 10 kHz. Sample temperature was maintained at 298 K within a precision of 10 mK. The  $^{31}\text{P}$  spectra were externally referenced to 0 ppm of  $^{31}\text{P}$  recorded separately in  $\text{H}_3\text{PO}_4$ .

### *Preparation of Ligand Treated $\text{CH}_3\text{NH}_3\text{PbI}_3$ Single Crystal Powder for Solid State NMR*

Lead iodide (98%) and anhydrous  $\gamma$ -butyrolactone ( $> 99\%$ ) were purchased from Sigma Aldrich and used without further purification. Methylammonium iodide (MAI) was synthesized by reacting methylamine (33 wt% in EtOH, Sigma) with equimolar hydriodic acid (57 wt%, Sigma) in an ice bath. The reaction mixture was stirred for 60 minutes and the liquid was removed with a rotary evaporator. The crude MAI solid was redissolved with EtOH ( $> 99.5\%$ , Sigma), then precipitated and washed with diethyl ether ( $> 99\%$ , Sigma). The MAI was dried and transferred to a nitrogen atmosphere. Our procedure for single crystal growth was based off of the inverse temperature crystallization (ITC) method of Saidaminov et al.<sup>4</sup> A 1.2 M solution of both  $\text{PbI}_2$  and MAI (1:1 molar ratio) was prepared in anhydrous  $\gamma$ -butyrolactone. The solution, exposed to ambient conditions, was preheated to 60 °C. Approximately 2 mL of this solution was filtered using a 0.2  $\mu\text{m}$  PTFE filter. The filtrate was added to a 4 mL vial which was sealed shut before submerging in an oil bath heated to 80 °C. Over the course of two days, the temperature of the oil bath was gradually increased to 110 °C. After the two days, a  $\sim 1\text{ cm}^3$   $\text{CH}_3\text{NH}_3\text{PbI}_3$  single crystal was removed from the growth solution and washed with two 2 mL aliquots of acetophenone. The crystal was then dried and transferred into a  $\text{N}_2$  filled glovebox. In the glovebox, the single crystal was ground into a very fine powder using a mortar and pestle and approximately 300 mg of the powder was transferred to a 10 mL centrifuge tube. The powder was then exposed to 1 mL of a 1 M  $\text{PPh}_3$  solution in CB. The  $\text{PPh}_3$ /perovskite powder mixture was vortexed for  $\sim 20$  seconds, then centrifuged for 3 minutes at 3000 rpm. The supernatant was discarded and the treated perovskite crystals were dried under  $\text{N}_2$  flow for  $\sim 2$  hours, the crystals were mixed with a spatula every 30 minutes to ensure uniform drying. Figure S7 shows X-ray diffraction patterns of the control and treated perovskite powders, which are consistent with previous reports.<sup>4</sup> The treated perovskite powder was then packed densely into the MAS rotor for solid-state NMR measurements.

### External Photoluminescence Quantum Efficiency (PLQE) Measurement

PLQE measurements were acquired using an integrating sphere setup (Hamamatsu C9920-02, A10094). A 532 nm CW laser (CrystaLaser, GCL532-005-L) was used to excite the sample and neutral density filters were used to attenuate the laser for intensity dependent measurements. Data acquisition followed the protocol describe by de Mello et al.,<sup>5</sup> with a scattering correction.

### Fluorescence Microscopy

Optical microscopy and spectroscopy were performed using a custom sample scanning confocal microscope built around a Nikon TE-2000 inverted microscope fitted with an infinity corrected 50x dry objective (Nikon L Plan, NA 0.7, CC 0-1.2). A 470 nm pulsed diode laser (PDL-800 LDH-P-C-470B, 300 ps pulse width) was used for excitation with repetition rate of 40 MHz. The emission was filtered through a 50/50 dichroic beamsplitter and a pair of 700 longpass filters. Photoluminescence from the sample was directed to a Micro Photon Devices (MPD) PDM Series single photon avalanche photodiode with a 50  $\mu$ m active area for TRPL measurements or a portable charge coupled device spectrometer (USB 2000, Ocean Optics) for steady state PL measurements. The sample stage was controlled using a piezo controller (Physik Instrumente E-710). For fluorescence microscopy, the pixel size was 100 nm with a pixel dwell time (integration time) of 50 ms. Before measurements, the system was calibrated using 200 nm fluorescent microspheres (Lifetechnologies FluoSpheres® Polystyrene Microspheres, 200 nm, red fluorescent, 580/605).

## Supplementary Figures and Text

### S.1 Photoluminescence Improvements Using Thiol and Amine Lewis Bases

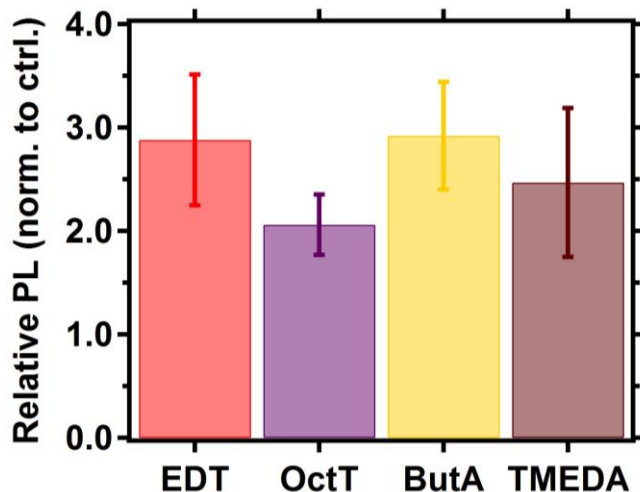


**Figure S1.** Integrated photoluminescence (PL) intensity enhancements for ethanedithiol (EDT), octanethiol (OctT), butylamine (ButA), and tetramethylethylenediamine (TMEDA) excited at 470 nm with fluences ranging from 15-80 nJ/cm<sup>2</sup> per pulse. The relative PL values on the left axis are the ratio of integrated PL intensities of treated to control samples, error bars are standard error of the mean for N=10.

Ligand	Structure	Concentration Range (M)
Ethanedithiol (EDT)		0.002 – 1
Octanethiol (OctT)		0.002 – 1
Butylamine (ButA)		0.008 – 0.01
Tetramethyl-ethylenediamine (TMEDA)		0.0008 – 0.003

**Table S1.** Ligand structures and concentration ranges of treatments not reported in the main text, but which also showed improvements in PL lifetime and intensity. In the structure column, yellow spheres denote sulfur atoms and purple spheres are nitrogen.

**S.2 Photoluminescence Improvements for Films with  $\text{PbCl}_2$  and  $\text{PbI}_2$  as Pb Source**

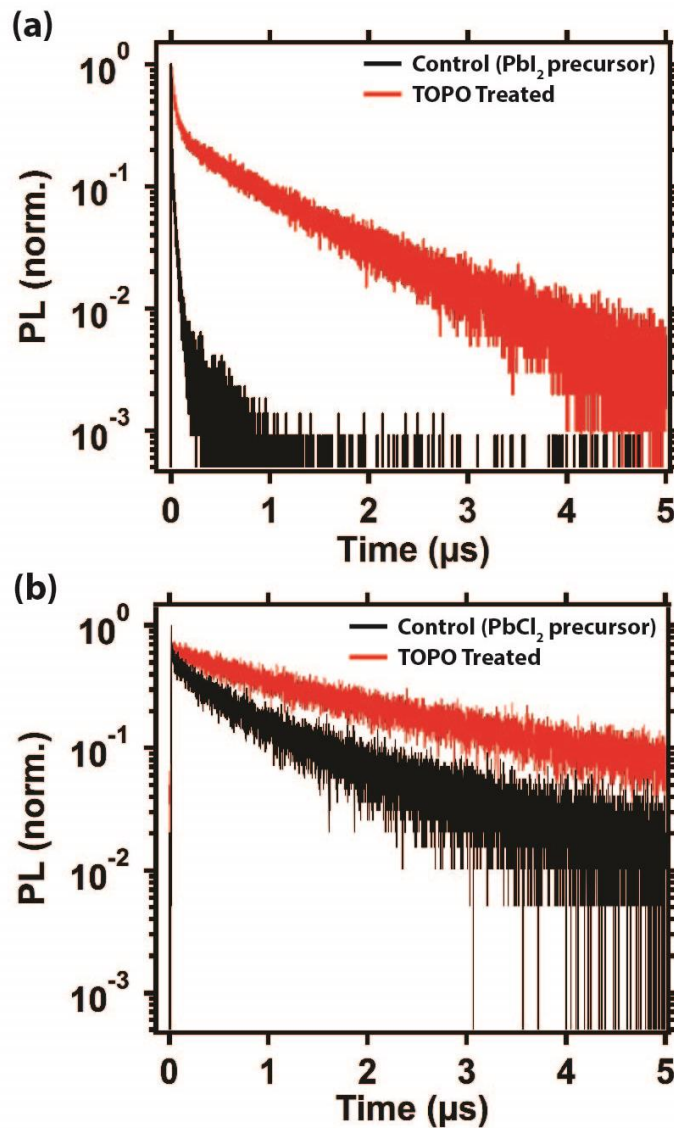


**Figure S2.** Bulk time-resolved photoluminescence of a (a)  $\text{CH}_3\text{NH}_3\text{PbI}_3$  thin film prepared from a  $\text{PbI}_2$  precursor and (b)  $\text{CH}_3\text{NH}_3\text{PbI}_3(\text{Cl})$  thin film prepared from a  $\text{PbCl}_2$  precursor before (black) and after treatment (red) with 0.005 M trioctylphosphine oxide (TOPO) in chlorobenzene. Samples were excited at 470 nm at a fluence of  $70 \text{ nJ/cm}^2$  per pulse.

### S.3 Photoluminescence Measurements of Samples Exposed to Treatment Solvent

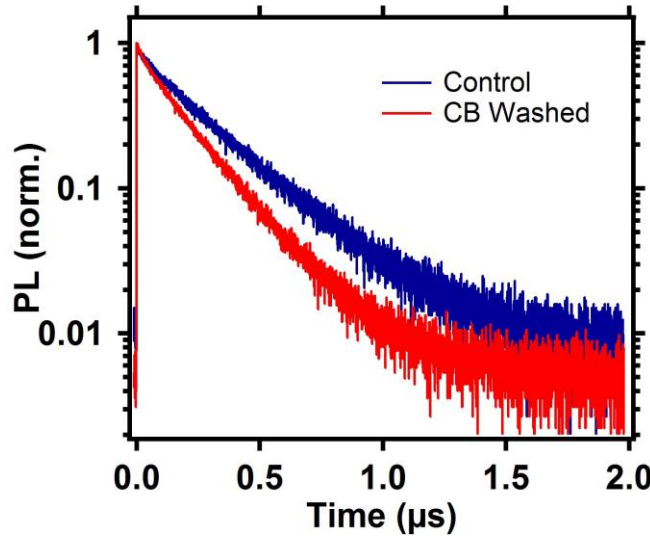


**Figure S3.** Bulk time-resolved photoluminescence of a control film (blue) and the same film after being washed with the treatment solvent (red), anhydrous chlorobenzene (CB), excited at 470 nm at a fluence of  $30 \text{ nJ/cm}^2$  per pulse. PL improvements are not observed without the surface ligands in the solution.

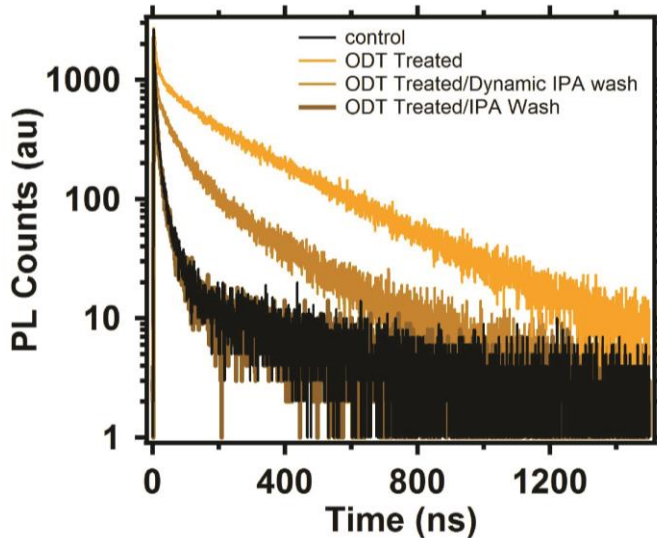


**Figure S4.** Time resolved photoluminescence decay traces of a control film (black) treated with octadecanethiol (ODT, bright orange), then dynamically washed with 2-propanol (IPA, orange) or regularly washed with IPA (brown). The dynamic wash retains some of the PL enhancement, whereas a regular wash removes the improvement entirely (See “Surface Treatment Deposition and Wash” in the Materials and Methods section).

**S.4 GDOES, SEM, UV-Vis Spectroscopy, and XRD Characterization of Ligand Treated Films**

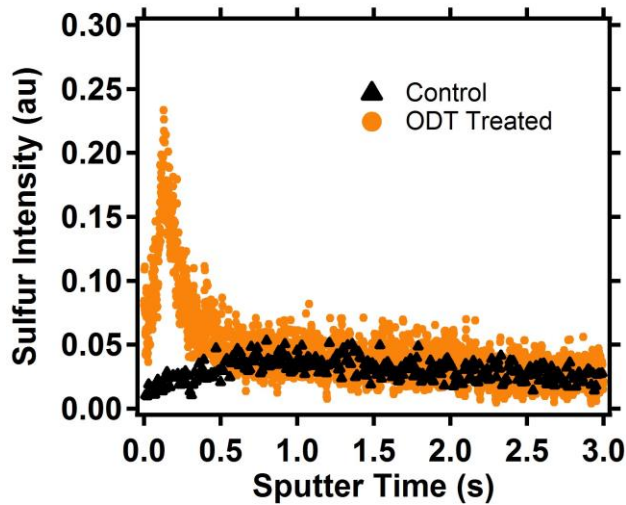


**Figure S5.** Glow discharge optical emission spectroscopy (GDOES) monitoring the sulfur intensity as a function of film depth of an untreated control film (black) and octadecanethiol (ODT) treated (orange) film.

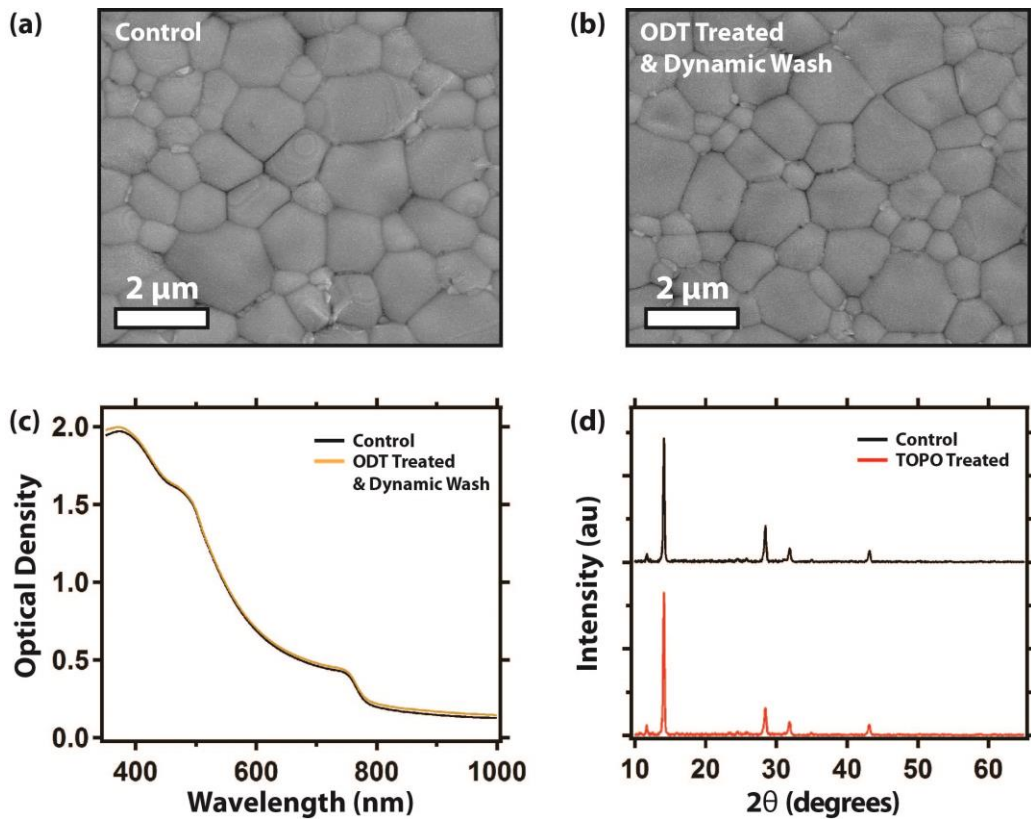


**Figure S6.** (a) Scanning electron microscope (SEM) images of a polycrystalline perovskite film before (a) and after (b) octadecanethiol (ODT) treatment and a subsequent dynamic wash with chlorobenzene, showing no observable restructuring of

the film morphology. (c) Linear absorption spectrum of a film before and after ODT treatment which underwent a dynamic wash with IPA. (d) Background subtracted X-ray diffraction patterns of a polycrystalline film before and after treatment with trioctylphosphine oxide (TOPO), showing no significant change in phase composition or crystallinity.

S.5 XRD Characterization of Control and Ligand Treated Single Crystal Perovskite ( $\text{CH}_3\text{NH}_3\text{PbI}_3$ ) Powders

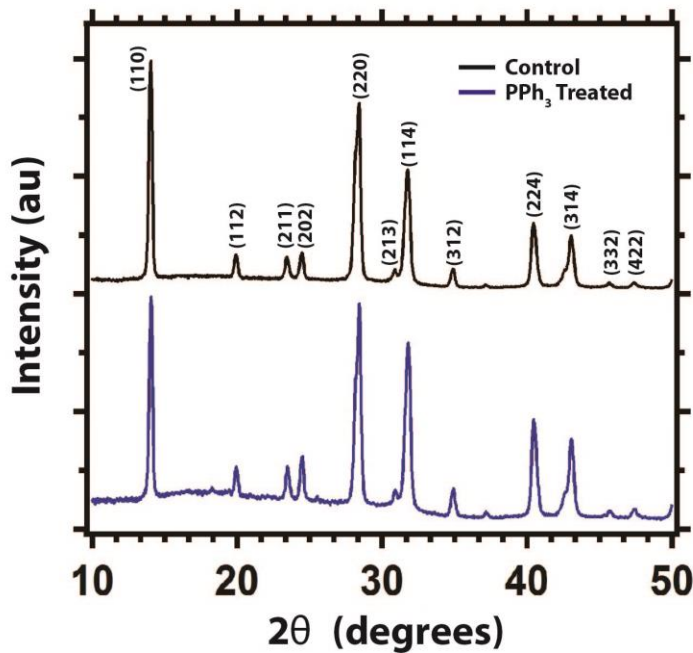


**Figure S7.** X-ray diffraction patterns of the single crystal powder before (black) and after treatment with triphenylphosphine (PPh<sub>3</sub>, blue), prepared for the solid-state NMR experiment (Figure 2c in the main article), small differences in peak intensities are attributed to heterogeneity in the prepared powders. The XRD pattern is consistent with previous reports of the tetragonal phase of  $\text{CH}_3\text{NH}_3\text{PbI}_3$ .<sup>4</sup>

### S.6 Calculation of Photoluminescence Decay Rate Constants

As a qualitative measure to confirm the observed changes in non-radiative decay between the control and TOPO treated samples, we model the PLQE data taking into account non-radiative and radiative monomolecular recombination, bimolecular recombination,<sup>6,7</sup> and Auger recombination,<sup>8</sup> according to equation S1:

$$PLQE = \frac{k_r N + k_b N^2}{k_{nr} N + k_r N + k_b N^2 + k_A N^3} \times 100\% \quad (S1),$$

Where  $k_{nr}$ ,  $k_r$ ,  $k_b$ , and  $k_A$  are the non-radiative monomolecular (trap-assisted), radiative monomolecular, bimolecular, and Auger recombination rate constants, respectively. We simulate and fit solutions to the data using equation S1 along with the experimentally measured excitation powers to obtain the generation rates (and hence carrier densities) for the fits. Under steady-state conditions the generation rate is equal to the total recombination rate. We report small variations in the fit parameters for the treated film:  $k_r = 3.8 \times 10^4 \text{ s}^{-1}$  and  $k_b = 4.0 \times 10^{-11} \text{ cm}^3 \text{ s}^{-1}$ , compared to the control film:  $k_r = 4.1 \times 10^4 \text{ s}^{-1}$  and  $k_b = 3.5 \times 10^{-11} \text{ cm}^3 \text{ s}^{-1}$  when we constrain  $k_A$  to  $4 \times 10^{-28} \text{ cm}^6 \text{ s}^{-1}$ , consistent with previous reports.<sup>9,10</sup> Whereas we observe  $k_{nr} = 9.1 \times 10^5 \text{ s}^{-1}$  for the TOPO treated film and  $k_{nr} = 6.6 \times 10^6 \text{ s}^{-1}$  for the control film. In Figure S9 we show the simulated solutions at carrier densities higher than those achieved in the PLQE experiments, showing a decrease in PLQE as the non-radiative Auger recombination begins to dominate at higher carrier densities, consistent with previous reports.<sup>8</sup>

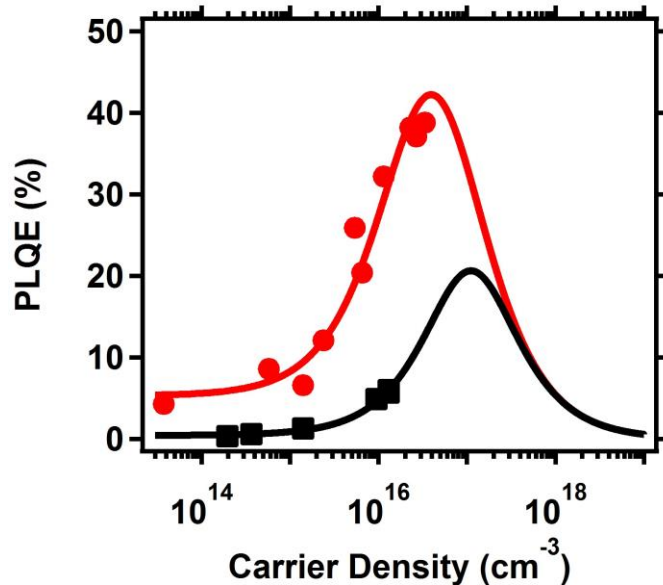


**Figure S8.** External PL quantum efficiency (PLQE) of the control (black) and TOPO treated films as a function of carrier density (532 nm, CW laser), reported in the main article as Figure 3c, but with x-axis as excitation power. Solid lines are fits to the data using the model described in equation S1.

### S.7 Photoluminescence Spectral Shift Induced by Ligand Treatment

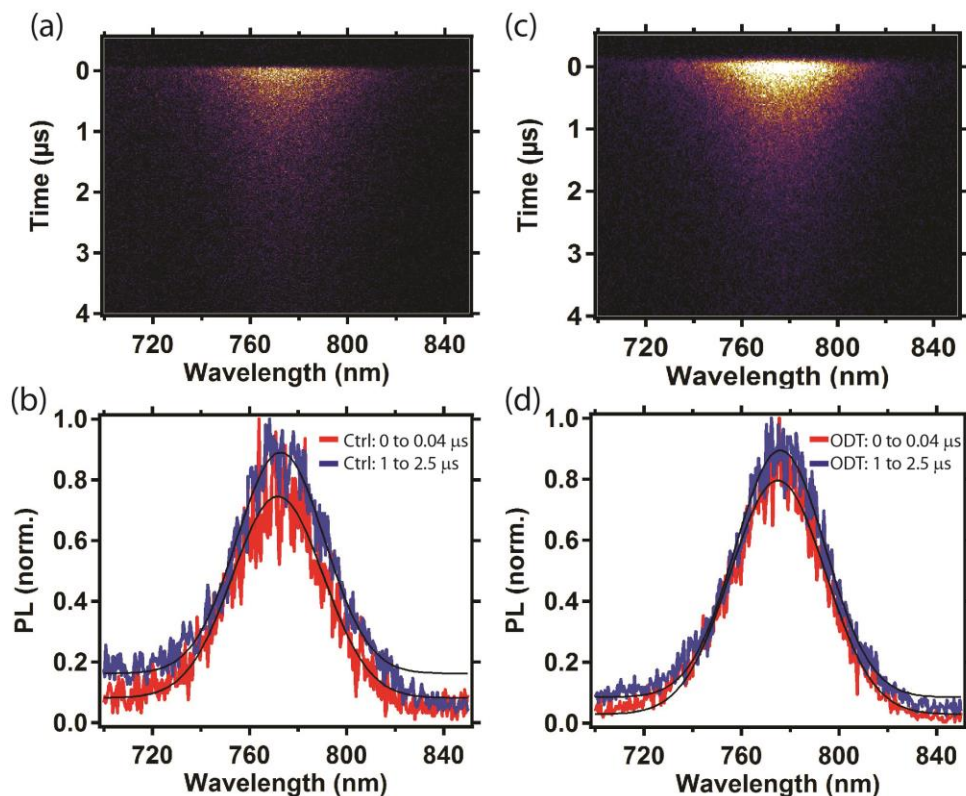


**Figure S9.** (a) Spectrally and temporally resolved PL emission of an untreated control film. (b) Time-integrated spectral slices from 0 to 40 ns and 1 to 2.5  $\mu$ s of control in (a). Solid lines are Gaussian fits to the PL spectra, with peaks centered at  $\sim$ 773 nm. (c) Spectrally and temporally resolved PL emission of an octadecanethiol (ODT) treated film. (d) Time integrated spectral slices from 0 to 40 ns and 1 to 2.5  $\mu$ s of the ODT treated film in (c). Solid lines are Gaussian fits to the PL spectra, with peaks centered at  $\sim$ 776 nm.

As briefly discussed in the main article, the spectral shift induced by ligand treatment could stem from several possibilities, including compositional changes at the grain boundaries, lattice strain, variations in crystallinity, and photon recycling.<sup>11-15</sup> To determine whether photon recycling contributes to the observed spectral shift, we performed temporally and spectrally resolved PL measurements with a streak camera setup. As Yamada et al. have previously reported for single crystal perovskite samples, photon recycling causes a slow spectral shift over the entire PL decay.<sup>14</sup> This is a result of the greater probability of higher energy photons being reabsorbed due to the greater spectral overlap with the absorption spectrum, this artificially red-shifts the observed spectrum compared to the true spectrum.<sup>13</sup> For single crystal samples, Yamada et al. observed a  $\sim$ 30 meV spectral shift over a 1  $\mu$ s time window. Here, we observe little to no spectral shifts in the control and treated films for representative time slices, which suggests that photon recycling does not significantly contribute to the ligand induced spectral changes.

### S.8 Fluorescence Image Characterization: Relative PL Intensity Changes of Grain Boundaries vs. Grain Interiors and Dark, Medium, vs. Bright Regions

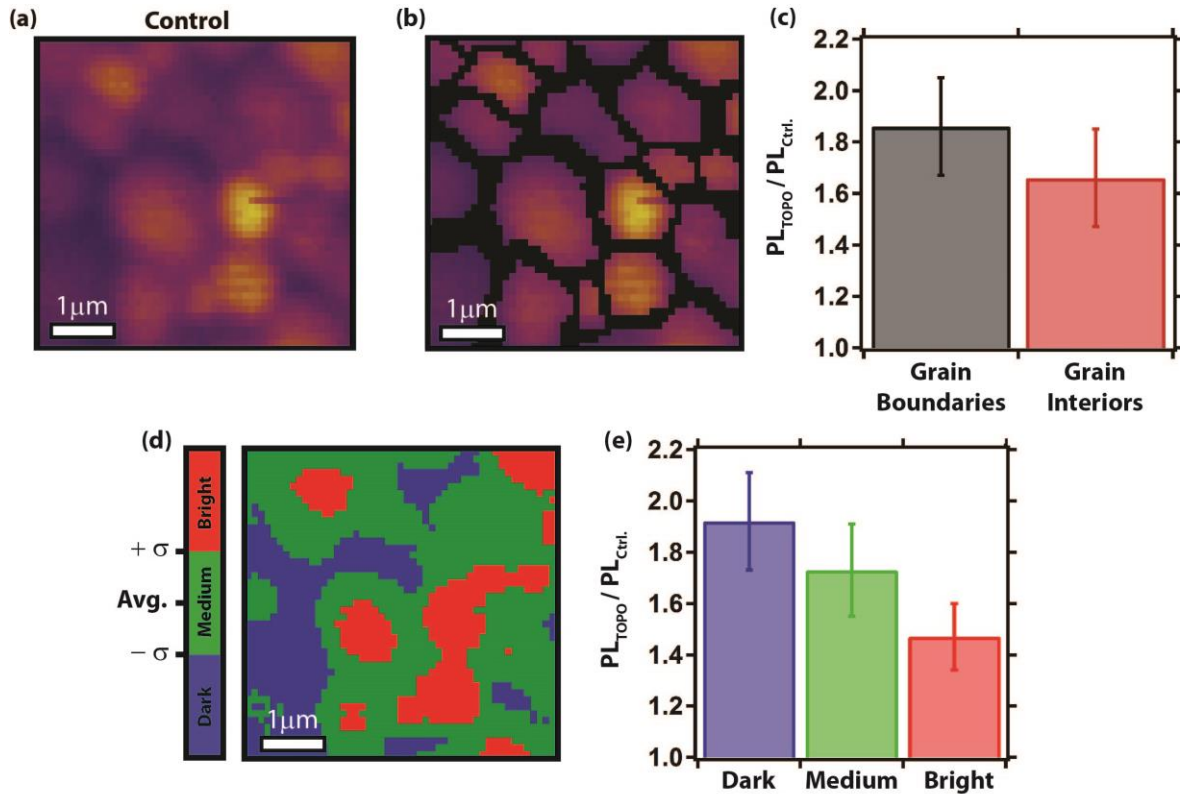


**Figure S10.** (a) Fluorescence image of the control film shown in Figure 4a in the main article before TOPO treatment and used as a reference to define separate grains and grain boundaries. (b) Image showing the regions that were manually defined as grain boundaries (black pixels) versus regions defined as grain interiors (colored pixels). (c) Average PL enhancements for grain boundaries (black) and grain interiors (red) using the pixel masks defined in (b) after TOPO treatment, errors bars are the standard deviations of the mean. (d) Three-color scale image showing the regions classified as dark (blue  $< -\sigma$  from average (avg.) PL intensity of control FI image (a)), medium ( $-\sigma \leq$  green  $\leq +\sigma$  from avg.) and bright (red  $> +\sigma$  from avg.). (e) Average PL enhancements for dark (blue), medium (green), and bright (red) regions defined in (d) after TOPO treatment, errors bars are the standard deviations of the mean. Regions that are initially dark have the largest relative improvements compared to the medium and bright regions after TOPO treatment.

In Figure S10, we analyze the relative improvements after TOPO treatment using two different definitions. In definition (1), we separate grains from grain boundaries by manually applying pixel masks to the images (Figure 10b). In Figure S10c, we report the average PL improvements of pixels that fall under these classifications by dividing the fluorescence image after TOPO treatment (Figure 4b in the main article) by the control

image (Figure S10a and 4a in the main article). Using definition (1), we report a larger improvement at the regions defined as grain boundaries as compared to grain interiors after TOPO treatment. In definition (2), we acknowledge that grain boundaries are not necessarily the regions with the lowest PL, consistent with our previous studies,<sup>7</sup> and therefore apply pixel masks based on the statistics of the image histogram. Following our previous study,<sup>16</sup> pixels which correspond to a PL intensity value that are  $< -\sigma$  from the average (avg.) PL intensity of the control FI image are defined as dark regions (which could encompass grain boundaries as well as entire grains). Medium and bright regions are also defined:  $-\sigma$  from the average  $\leq$  medium  $\leq +\sigma$  from the average, and bright  $> +\sigma$  from the average. These definitions allow for an objective evaluation of the relative improvements of various regions depending on their initial PL. In Figure S10e, we report the average PL improvements of pixels that fall under these classifications by dividing the fluorescence image after TOPO treatment (Figure 4b in the main article) divided by the control image (Figure S10a and 4a in the main article). Using definition (2), we report a larger improvement at the regions defined as “dark” as compared to “bright”. Interestingly, we note that many (but not all) dark pixels in Figure S10d also correspond to grain boundaries in Figure S10b.

## References

- (1) Zhang, W.; Saliba, M.; Moore, D. T.; Pathak, S. K.; Horantner, M. T.; Stergiopoulos, T.; Stranks, S. D.; Eperon, G. E.; Alexander-Webber, J. A.; Abate, A. *et al.* Ultrasmooth Organic-Inorganic Perovskite Thin-Film Formation and Crystallization for Efficient Planar Heterojunction Solar Cells. *Nat. Commun.* **2015**, *6*, 6142.
- (2) Lee, M. M.; Teuscher, J.; Miyasaka, T.; Murakami, T. N.; Snaith, H. J. Efficient hybrid solar cells based on meso-superstructured organometal halide perovskites. *Science* **2012**, *338*, 643-647.
- (3) Jeon, N. J.; Noh, J. H.; Kim, Y. C.; Yang, W. S.; Ryu, S.; Seok, S. I. Solvent engineering for high-performance inorganic-organic hybrid perovskite solar cells. *Nat. Mater.* **2014**, *13*, 897-903.
- (4) Saidaminov, M. I.; Abdelhady, A. L.; Murali, B.; Alarousu, E.; Burlakov, V. M.; Peng, W.; Dursun, I.; Wang, L.; He, Y.; Maculan, G. *et al.* High-Quality Bulk Hybrid Perovskite Single Crystals Within Minutes by Inverse Temperature Crystallization. *Nat. Commun.* **2015**, *6*, 7586.
- (5) de Mello, J. C.; Wittmann, H. F.; Friend, R. H. An improved experimental determination of external photoluminescence quantum efficiency. *Adv. Mater.* **1997**, *9*, 230-232.
- (6) Stranks, S. D.; Burlakov, V. M.; Leijtens, T.; Ball, J. M.; Goriely, A.; Snaith, H. J. Recombination Kinetics in Organic-Inorganic Perovskites: Excitons, Free Charge, and Subgap States. *Phys. Rev. Appl.* **2014**, *2*, 034007.
- (7) deQuilettes, D. W.; Vorpahl, S. M.; Stranks, S. D.; Nagaoka, H.; Eperon, G. E.; Ziffer, M. E.; Snaith, H. J.; Ginger, D. S. Impact of Microstructure on Local Carrier Lifetime in Perovskite Solar Cells. *Science* **2015**, *348*, 683-686.
- (8) Johnston, M. B.; Herz, L. M. Hybrid Perovskites for Photovoltaics: Charge-Carrier Recombination, Diffusion, and Radiative Efficiencies. *Acc. Chem. Res.* **2016**, *49*, 146-154.
- (9) Trinh, M. T.; Wu, X.; Niesner, D.; Zhu, X. Y. Many-Body Interactions in Photo-Excited Lead Iodide Perovskite. *J. Mater. Chem. A* **2015**, *3*, 9285-9290.
- (10) Saba, M.; Cadelano, M.; Marongiu, D.; Chen, F.; Saritzu, V.; Sestu, N.; Figus, C.; Aresti, M.; Piras, R.; Lehmann, A. G. *et al.* Correlated Electron-Hole Plasma in Organometal Perovskites. *Nat. Commun.* **2014**, *5*, 5049.
- (11) Nie, W.; Tsai, H.; Asadpour, R.; Blancon, J. C.; Neukirch, A. J.; Gupta, G.; Crochet, J. J.; Chhowalla, M.; Tretiak, S.; Alam, M. A. *et al.* High-Efficiency Solution-Processed Perovskite Solar Cells with Millimeter-Scale Grains. *Science* **2015**, *347*, 522-525.
- (12) D'Innocenzo, V.; Srimath Kandada, A. R.; De Bastiani, M.; Gandini, M.; Petrozza, A. Tuning the Light Emission Properties by Band Gap Engineering in Hybrid Lead Halide Perovskite. *J. Am. Chem. Soc.* **2014**, *136*, 17730-17733.
- (13) Pazos-Outon, L. M.; Szumilo, M.; Lamboll, R.; Richter, J. M.; Crespo-Quesada, M.; Abdi-Jalebi, M.; Beeson, H. J.; Vrucinic, M.; Alsari, M.; Snaith, H. J. *et al.* Photon Recycling in Lead Iodide Perovskite Solar Cells. *Science* **2016**, *351*, 1430-1433.
- (14) Yamada, Y.; Yamada, T.; Phuong, L. Q.; Maruyama, N.; Nishimura, H.; Wakamiya, A.; Murata, Y.; Kanemitsu, Y. Dynamic Optical Properties of  $\text{CH}_3\text{NH}_3\text{PbI}_3$

Single Crystals As Revealed by One- and Two-Photon Excited Photoluminescence Measurements. *J. Am. Chem. Soc.* **2015**, *137*, 10456-10459.

(15) Wu, B.; Nguyen, H. T.; Ku, Z.; Han, G.; Giovanni, D.; Mathews, N.; Fan, H. J.; Sum, T. C. Discerning the Surface and Bulk Recombination Kinetics of Organic-Inorganic Halide Perovskite Single Crystals. *Adv. Energy Mater.* **2016**, *1600551*.

(16) deQuilettes, D. W.; Zhang, W.; Burlakov, V. M.; Graham, D. J.; Leijtens, T.; Osherov, A.; Bulovic, V.; Snaith, H. J.; Ginger, D. S.; Stranks, S. D. Photo-Induced Halide Redistribution in Organic-Inorganic Perovskite Films. *Nat. Commun.* **2016**, *7*, 11683.